Ultramicroscopy 109 (2009) 154–160

Contents lists available at ScienceDirect

Ultramicroscopy

journal homepage: www.elsevier.com/locate/ultramic

Relativistic effects in elastic scattering of electrons in TEM

Axel Rother [a,*], Kurt Scheerschmidt [b]

[a] Triebenberg Laboratory, Institute of Structure Physics, Technische Universitaet Dresden,D-01062 Dresden, Germany
[b] Max Planck Institute of Microstructure Physics, Weinberg 2, D-06120 Halle, Germany

ARTICLE INFO

Article history:
Received 10 January 2008
Received in revised form
14 August 2008
Accepted 29 August 2008

PACS:
61.05jd
61.05jp
42.25Fx

Keywords:
Electron diffraction
High-resolution TEM
Electron holography

ABSTRACT

Transmission electron microscopy typically works with highly accelerated thus relativistic electrons. Consequently the scattering process is described within a relativistic formalism. In the following, we will examine three different relativistic formalisms for elastic electron scattering: Dirac, Klein-Gordon and approximated Klein-Gordon, the standard approach. This corresponds to a different consideration of spin effects and a different coupling to electromagnetic potentials. A detailed comparison is conducted by means of explicit numerical calculations. For this purpose two different formalisms have been applied to the approaches above: a numerical integration with predefined boundary conditions and the multislice algorithm, a standard procedure for such simulations. The results show a negligibly small difference between the different relativistic equations in the vicinity of electromagnetic potentials, prevailing in the electron microscope. The differences between the two numeric approaches are found to be small for small-angle scattering but eventually grow large for large-angle scattering, recorded for instance in high-angle annular dark field.

1. Introduction

Modern transmission electron microscopes (TEM) typically operate at acceleration voltages between 80 and 300 kV leading to projectile electron velocities between 0.5 and 0.78*c*, which are far above the non-relativistic regime. The imaging process, particularly in high-resolution TEM (HRTEM), can be regarded as a mapping of a plethora of electron–specimen interactions in a two-dimensional detector plane. The parameter space of the interaction is at least three-dimensional, whereas that of the detected image is only two-dimensional. Thus, the mapping is an injective one. In order to extract quantitative data about the specimen out of the high-resolution images, one has to confine the extracted data, e.g. asking only for the two-dimensional thickness profile, or expanding the collected data, for instance by employing electron tomography (e.g. [1]). To analyze a restricted number of specimen properties one uses electron scattering simulations with a restricted number of independent parameters, e.g. thickness or tilt of the specimen, for a refinement procedure with respect to the experimentally recorded images. Consequently an accurate scattering simulation is crucial for a successful refinement. The standard algorithms used for electron scattering simulations rely on an approximated scalar relativistic formalism [2]. In this work, we will examine the effects introduced by completely solving the Dirac equation under different constraints. Ferwerda et al. [3] and Jagannathan [4] investigated the implications of a fully relativistic treatment on the electron-optical imaging process; we will concentrate on the fully relativistic treatment of elastic electron–specimen scattering.

The dominant factor in the interaction process is the electrostatic potential of the specimen. Here the static, i.e. time independent, nature is inflicted by the low velocity of the specimen constituents compared to that of the incident electron. Inelastic interaction (e.g. [5,6]) will be omitted in the following analysis; it is, however, exploited by various methods to get additional information about the specimen (e.g. [7]). In the following sections two fully relativistic formalisms for elastic scattering simulations are deduced, making use of as few approximations as possible:

1. A numerical integration of the Dirac equation under particular boundary conditions (Section 3).
2. A predefined integration of the Dirac equation based on the multislice (MS) algorithm (Section 5).

Furthermore, the connections to two scalar relativistic approaches, Klein-Gordon and the standard formalism [2], essentially a solution of an approximated Klein-Gordon equation, will be shown (Section 4). The results of explicit numerical scattering

* Corresponding author.
E-mail address: Axel.Rother@triebenberg.de (A. Rother).

0304-3991/$ - see front matter © 2008 Elsevier B.V. All rights reserved.
doi:10.1016/j.ultramic.2008.08.008

calculations incorporating different electromagnetic potentials presented in Section 6 indicate a negligible difference between the different relativistic formalisms and a rather larger error of the MS Algorithm at large-angle scattering.

2. Relativistic description of the scattering and imaging process

We begin with some well known results for fully relativistic scattering like scattering cross sections to give an outlook to additional effects occurring through a fully relativistic description in comparison to scalar relativistic ones. The single particle Dirac equation is the starting point of all considerations following:

$$E\mathbf{\Psi}(\vec{r}) = [c\vec{\alpha}\cdot\widehat{\vec{p}} + mc^2\beta + V(\vec{r})]\mathbf{\Psi}(\vec{r}), \tag{1}$$

where E denotes the energy, c the velocity of light, m the rest mass of the electron, V the electrostatic potential, $\vec{\alpha}$ and β the Dirac matrices, $\widehat{\vec{p}}$ the momentum operator and $\vec{r}$ the three-dimensional space coordinate. The differential scattering cross sections $\mathrm{d}\sigma/\mathrm{d}\Omega$ derived from Eq. (1) for an unpolarized electron beam on an atom core with charge Z (no momentum transfer to the core) is described by the famous Mott formula (e.g. [8]):

$$\frac{\mathrm{d}\sigma}{\mathrm{d}\Omega}(\theta) = \frac{Z^2\alpha_s^2\left(1-\beta_r^2\sin^2\frac{\theta}{2}\right)}{4\beta_r^2|\vec{p}|^2\sin^4\frac{\theta}{2}}. \tag{2}$$

Here, α_s denotes the Sommerfeld fine structure constant and β_r the quotient of the projectile particle velocity with the speed of light. In the limit of small velocities $v/c=\beta_r \ll 1$ or small scattering angles θ (2) becomes

$$\frac{\mathrm{d}\sigma}{\mathrm{d}\Omega}(\theta) = \frac{Z^2\alpha_s^2}{4\beta_r^2|\vec{p}|^2\sin^4\frac{\theta}{2}}, \tag{3}$$

which is the Rutherford cross section (e.g. [8]), derived from the Klein-Gordon equation. The additional term in Eq. (2) only affects large-angle scattering, i.e. scattering angles of 200 mrad (only recorded in high-angle diffraction techniques like high-angle annular dark field (HAADF) TEM) differ about 1.15% at 200 kV, with already small differential cross sections. Consequently, only small effects are expected due to a fully relativistic description in the case of scattering on electrostatic potentials. The scattering on magnetostatic potentials can be discussed on the basis of an alternative form of the Dirac equation [6,9]

$$[(E-V)^2 - c^2\widehat{\vec{p}}^2 - m^2c^4 - \mathrm{i}e\hbar c\vec{E}\cdot\vec{\alpha} - e\hbar c^2\vec{B}\cdot\vec{\sigma}]\mathbf{\Psi} = 0, \tag{4}$$

which shows the relationship of the Dirac equation to the scalar relativistic Klein-Gordon equation. Here $\vec{\sigma}$ denote the four-dimensional spin matrices and e the unit charge. By neglecting the last two terms in the brackets one ends up with four decoupled Klein-Gordon equations:

$$[(E-V)^2 - c^2\widehat{\vec{p}}^2 - m^2c^4]\Psi = 0. \tag{5}$$

The validity of this step depends on the strength of the two electromagnetic field terms relative to the other terms in Eq. (4). The electric field in the vicinity of an atom core diverges strongly with $1/r^2$, making the fourth term in Eq. (4) eventually larger than the other ones. Since this region close to the atom core is very small, the approximation is indeed possible though, in particular when considering small-angle scattering only. This is verified by the small difference between the two cross sections given above and the numerical calculations in Section 6. Strong magnetic fields however can possibly couple more significantly the different parts of the spinor, due to an additional factor of c in the coupling term containing the magnetic field $\vec{B}$. The magnitude of the coupling can be estimated by inserting a typical value for atomic scale magnetic fields present in ferromagnetic solids of 100 T in Eq. (4)

$$|e\hbar c^2\vec{B}\cdot\vec{\sigma}| \approx 5600\ (\mathrm{eV})^2,$$

which is of the same order of magnitude like the kinetic terms perpendicular to the beam direction. These strong magnetic fields, produced by the localized spin current density of partly filled shells, are divergent free and strongly rotating, thus changing direction in each unit cell. Consequently the average magnetic field in ferromagnetic solids is much lower, reaching several Tesla at maximum. In Section 6 we will therefore test the influence of magnetic fields produced by a deliberately chosen ferromagnet: α-Fe.

If the scattering result depends on the spin of the projectile electron, the imaging process has to be reformulated fully relativistically as well. In a simple approximation neglecting effects like the smearing out of the signal by the transfer properties of the detector, the recorded signal in the detector plane $\vec{R}$ is the density of the incoming electron wave. The electron density of a Dirac wave is $\rho = \mathbf{\Psi}^\dagger\mathbf{\Psi} = \sum_{n=1}^{4}|\mathbf{\Psi}_n(\vec{R})|^2$. Generally, 2D quantities, e.g. those in the detector plane, will be denoted by big letters contrary to small lettered 3D quantities. The scalar product $\mathbf{\Psi}^\dagger\mathbf{\Psi}$ couples only similar parts of the spinor, i.e. a scalar product between one spin up and one spin down spinor vanishes. A spin dependent scattering with possibly strong spin–orbit coupling would consequently influence the recorded signal. Additional differences occur between conventional imaging and off-axis electron holography. The signal recorded in off-axis holography is

$$\begin{aligned}\rho(\vec{R}) &= \sum_{n=1}^{4}|\Psi_n(\vec{R}) + U_n\,\mathrm{e}^{\mathrm{i}\vec{K}_0\vec{R}}|^2 \\ &= 1 + \sum_{n=1}^{4}(|\Psi_n(\vec{R})|^2 + \Psi_n(\vec{R}U_n\,\mathrm{e}^{-\mathrm{i}\vec{K}_0\vec{R}} + \Psi_n^*(\vec{R})U_n\,\mathrm{e}^{\mathrm{i}\vec{K}_0\vec{R}}).\end{aligned}$$

Here $\mathbf{U}$ is a constant four-component spinor denoting the spin state of the reference wave. The second term on the right hand side represents the conventional TEM image. The third and the fourth term are mutually conjugate-complex; they are referred to as sidebands, representing the recorded image wave in Fourier space. One of the sidebands is used to reconstruct the complete wave $\mathbf{\Phi}_{\mathrm{rec}}$ by amplitude and phase:

$$\mathbf{\Phi}_{\mathrm{rec}} = \sum_{n=1}^{4}\Psi_n U_n.$$

This expression demonstrates that when using spin polarized electrons, i.e.

$$\mathbf{U} = \frac{1}{\sqrt{1+\left(\frac{c\hbar k_0}{mc^2+E}\right)^2}}\begin{pmatrix}1\\0\\c\hbar k_0/(mc^2+E)\\0\end{pmatrix},$$

the parts of the electrons scattered in Ψ_2 and Ψ_4 do not contribute to the interference pattern recorded in the sidebands and therefore attenuate the contrast. As indicated above spin dependent scattering will turn out to be very weak though, suppressing the implications from a fully relativistic imaging process.

3. Elastic scattering in the forward scattering approximation

The setup of the scattering experiment is depicted in Fig. 1. The incident electron moves in z-direction and eventually impinges on the specimen, where it is scattered into all directions. Due to the special experimental setup when recording high-resolution

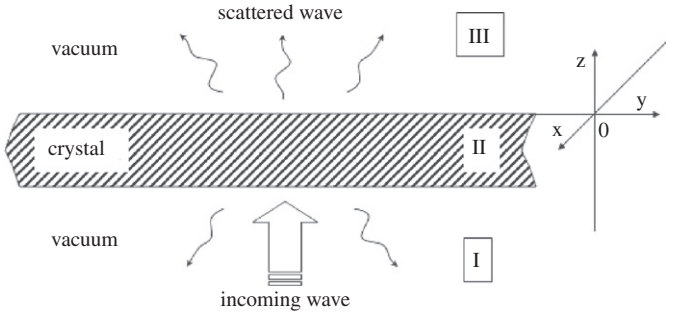

Fig. 1. Scheme of electron–specimen scattering including coordinate system.

images, the spatial extension of the recorded object exit wave (20 nm) is small compared to the extension of both, the specimen and incident coherent wave packet describing the electron. One can therefore apply periodic boundary conditions in *xy*-directions, keeping only the *z*-extension of the specimen finite.

Furthermore, the wave packet can be approximated by a plane wave under normal imaging conditions. The problem of solving the Dirac equation within those boundary conditions is now tackled by assuming that the solution of the Dirac equation at the incident plane is already known, being the incident plane wave. The pin pointing of the boundary conditions at the entrance face to the incoming wave is referred to as the forward scattering approximation [5], since no back-scattered electrons occur within this approach. It is phenomenologically verified by the large incident velocity of the electrons and the small thickness of the specimen, giving rise to scattering angles only in forward direction. A strict mathematical verification however would require a solution to Eq. (1) without pin-pointed boundary conditions, but with the continuity equation at the specimen entrance and exit face fulfilled. This has been conducted by Lamla for the Schrödinger equation [10], the corresponding analysis for the Dirac equation, however, is still missing. Nevertheless, the forward scattering approximation renders a formulation of the Dirac equation as a coupled set of ordinary differential equations possible, which can be solved numerically by standard algorithms (e.g. Runge-Kutta [11]). Firstly one writes both, the electromagnetic potentials and the spinor, as a Fourier series in the *xy*- or $\vec{R}$-plane with the 2D reciprocal space denoted by $\vec{G}$. This requires, however, the periodicity of both the electrostatic and the vector potential. The expansion of the wave function is possible due to the Bloch theorem applied to the Dirac equation [12]:

$$V(\vec{r}) = \sum_{\vec{G}} V(\vec{G},z)\, \mathrm{e}^{\mathrm{i}\vec{G}\vec{R}}, \tag{6}$$

$$\vec{A}(\vec{r}) = \sum_{\vec{G}} \vec{A}(\vec{G},z)\, \mathrm{e}^{\mathrm{i}\vec{G}\vec{R}}, \tag{7}$$

$$\mathbf{\Psi}(\vec{r}) = \sum_{\vec{G}} \mathbf{\Psi}(\vec{G}-\vec{K}_0,z)\, \mathrm{e}^{\mathrm{i}(\vec{G}-\vec{K}_0)\vec{R}}. \tag{8}$$

In the next step, for the sake of simplicity, we set the incident beam direction $\vec{K}_0$ to zero and insert the expressions (6)–(8) in Eq. (1) to get

$$E\mathbf{\Psi}(\vec{G}) = \Big[\hbar c\vec{\alpha}_{\vec{R}}\cdot\vec{G} - c\vec{\alpha}\cdot\vec{A}(\vec{G},z)\otimes - \mathrm{i}\hbar c\alpha_z\frac{\partial}{\partial z} + mc^2\beta + V(\vec{G},z)\otimes\Big]\mathbf{\Psi}(\vec{G}), \tag{9}$$

since the coefficients of every plane wave must be equal on each side of Eq. (9). The $\otimes$ denotes a convolution with the wave function outside of the brackets. Multiplying with $-\mathrm{i}\alpha_z/(\hbar c)$ and using $\alpha_z^2 = -1$ Eq. (9) can now be transformed to

$$\frac{\partial\mathbf{\Psi}(\vec{G},z)}{\partial z} = -\mathrm{i}\alpha_z\Big(\vec{\alpha}_{\vec{R}}\cdot\Big(\vec{G}-\frac{1}{\hbar}\vec{A}_{\vec{R}}(\vec{G},z)\otimes\Big) - \frac{1}{\hbar}\alpha_z \cdot A_z(\vec{G},z)\otimes + \frac{mc\beta}{\hbar} - \frac{E}{c\hbar} + \frac{1}{c\hbar}V(\vec{G},z)\otimes\Big)\mathbf{\Psi}(\vec{r}). \tag{10}$$

These are four coupled ordinary differential equations of the first order, which can be solved numerically providing the boundary conditions, i.e. the possibly spin polarized plane wave at the entrance face of the crystal. The approach outlined above for casting the Dirac equation into a set of coupled ordinary differential equations can be used in the same manner for the Klein-Gordon case. Again one makes use of the expansions (6), (7) and (8), being aware that the wave function $\Psi(\vec{r})$ is now a scalar one, and inserts them into the Klein-Gordon equation (5). Performing the same steps like in the Dirac case one gets

$$\Big[-c^2\hbar^2\frac{\partial^2}{\partial z^2} - 2\mathrm{i}c^2\hbar A_z(\vec{G},z)\otimes\frac{\partial}{\partial z}\Big]\Psi(\vec{G},z) = \Big[E^2 - 2EV(\vec{G},z)\otimes + V^2(\vec{G},z)\otimes - c^2A_z^2(\vec{G},z)\otimes - c^2\hbar^2\Big(\vec{G}-\frac{1}{\hbar}\vec{A}_{\vec{R}}(\vec{G},z)\Big)^2\otimes - m^2c^4\Big]\Psi(\vec{G},z), \tag{11}$$

which is again a set of ordinary coupled differential equations of the second order this time. One can however reduce the order to the first by doubling the number of equations. These equations can again be solved providing explicitly the boundary conditions at the entrance face, using standard numerical algorithms. The two relativistic formulations Eqs. (10) and (11) will be used to perform numerical calculations in Section 6. They rely only on the forward scattering approximation, thus providing a reference solution for more stringent approximations, developed in the next two sections.

4. The standard approach: the approximated Klein-Gordon equation

In the very beginning of electron scattering simulations it has been demonstrated, that relativistic effects occurring due to the relativistic velocities can be considered by applying a so-called relativistic correction to the Schrödinger equation (e.g. [5]). We will give a short derivation, which will shed some light on the approximation. We start again with the stationary Dirac equation and neglect in the first step spin contributions (see Eq. (4)), ending up with a Klein-Gordon equation:

$$[(E-V)^2 - c^2\hat{\vec{p}}^2 - m^2c^4]\Psi = 0. \tag{12}$$

Now we assume, that the electrostatic potential V is small compared to the total energy E, i.e. $V \ll 2E$. That means we can neglect V^2 in Eq. (12), yielding

$$[E^2 - m^2c^4]\Psi = [2EV + c^2\hat{\vec{p}}^2]\Psi. \tag{13}$$

Inserting $E = \gamma mc^2$ with $\gamma = (1 - v^2/c^2)^{-1}$ into Eq. (13) and performing some rearrangements, one gets

$$\left[\frac{E^2 - m^2c^4}{2\gamma mc^2}\right]\Psi = \left[\frac{\hat{\vec{p}}^2}{2\gamma m} + V\right]\Psi = \left[-\frac{\hbar^2\Delta}{2\gamma m} + V\right]\Psi.$$

This is exactly the so-called relativistically corrected Schrödinger equation, i.e. both the rest mass m of the electron and the wave length are relativistically corrected. We would prefer to continue calling it approximated Klein-Gordon equation, since the

approximation applied was to neglect the squared part of the electrostatic potential and no $1/c$ expansion, usually termed as relativistic correction (e.g. [12]). The assumption $V \ll 2E$ is usually valid in the case of electrostatic potentials, produced by the deflectors of the microscope. The electrostatic potential of a single atom within the specimen, however, shows a Z/r asymptote close to the atom core. Hence, the assumption eventually fails in the vicinity of atom cores, especially when the atomic number Z is large. It is difficult to assess the error introduced by this approximation analytically. In Section 6 we will therefore examine the effect by comparing the standard approach to the Dirac (10) and Klein-Gordon (11) equation in explicit numerical calculations.

5. Relativistic multislice

Although being solvable, Eqs. (10), (11) and (11) without V^2 are of limited applicability since they need large computer power for the solution of a typical problem in high-resolution image simulation. We will therefore apply further approximations to the solution of the relativistic equations within the forward scattering approximation, ending finally at an algorithm very similar to the MS algorithm, presently used in scattering simulations (e.g. [13]). We start with the Dirac equation (4) and rewrite it by using the ansatz $\mathbf{\Psi}(\vec{r}) = \mathbf{\Phi}(\vec{r})\mathbf{U}e^{ik_0 z}$, separating the incident plane wave $\mathbf{U}\,e^{ik_0 z}$

$$0 = \Big[EV - V^2 + c^2\hbar^2\Delta_{\vec{R}} - 2ic^2\hbar\vec{A}_{\vec{R}}\cdot\vec{\nabla}_{\vec{R}} - c^2\vec{A}^2 + c^2\hbar^2\frac{\partial^2}{\partial z^2} + 2ic^2\hbar^2 k_0\frac{\partial}{\partial z} + 2ic^2\hbar A_z\frac{\partial}{\partial z} - c^2\hbar k_0 A_z - ie\hbar c\vec{E}\cdot\vec{\alpha} - e\hbar c^2\vec{B}\cdot\vec{\sigma}\Big]\mathbf{\Phi}(\vec{R}, z). \quad (14)$$

Given a large acceleration voltage, k_0 becomes large and one can make the assumptions that $\partial^2\Phi/\partial z^2 \ll k_{0z}\partial\Phi/\partial z$ and $A_z\partial/(\partial z) \ll k_0 A_z$. Consequently the two small terms can be omitted. This is equivalent to assuming that the incident wave is mainly scattered into a small angle around the incident direction and hence, the approximation is called small-angle approximation (e.g. [5]). Again, we cannot prove the correctness of this assumption at this stage, since this proof would involve the knowledge of the exact $\mathbf{\Phi}(\vec{r})$ as a solution of Eq. (14). We will therefore perform scattering simulations based on the exact expressions (10), Eqs. (11) and (11) without V^2 and compare them to simulations based on the solution of Eq. (14) in the forward scattering approximation. If they agree, we can show the correctness of this assumption. Neglecting $\partial^2/\partial z^2$ and $A_z\partial/(\partial z)$, we get after some rearrangements

$$\frac{\partial}{\partial z}\mathbf{\Phi}(\vec{R}, z) = \frac{i[EV - V^2 - c^2\vec{A}^2 + c^2\hbar^2\Delta_{\vec{R}} - 2ic^2\hbar\vec{A}_{\vec{R}}\cdot\vec{\nabla}_{\vec{R}} - c^2\hbar k_0 A_z - ie\hbar c\vec{E}\cdot\vec{\alpha} - e\hbar c^2\vec{B}\cdot\vec{\sigma}]}{2c^2\hbar^2 k_{0z}}\mathbf{\Phi}(\vec{R}, z). \quad (15)$$

The solution of Eq. (15) can be formally written as

$$\mathbf{\Phi}(\vec{R}, z+\Delta z) = \hat{T}_z \exp\left(\frac{i\int_z^{z+\Delta z}[EV - V^2 - c^2\vec{A}^2 + c^2\hbar^2\Delta_{\vec{R}} - 2ic^2\hbar\vec{A}_{\vec{R}}\cdot\vec{\nabla}_{\vec{R}} - c^2\hbar k_0 A_z - ie\hbar c\vec{E}\cdot\vec{\alpha} - e\hbar c^2\vec{B}\cdot\vec{\sigma}]dz'}{2c^2\hbar^2 k_{0z}}\right)\mathbf{\Phi}(\vec{R}, z), \quad (16)$$

by using the z-ordering operator $\hat{T}_z$. If the exponent in Eq. (16) is sufficiently small the different operators in the exponent can be separated according to the Baker-Campbell-Hausdorff formula $e^{\varepsilon(\hat{A}+\hat{B})} = e^{\varepsilon\hat{A}}e^{\varepsilon\hat{B}}e^{\mathcal{O}(\varepsilon^2)}$ ($\hat{A}$ and $\hat{B}$ denote arbitrary operators) [13]. To assure the smallness of the exponent, the intervals Δz have to be determined accordingly. Furthermore, the smallness of Δz makes the differential operators in the exponent approximately independent from the z-coordinate, hence the z-ordering operator $\hat{T}_z$ can be dropped. Finally, if we make use of Bloch's theorem again and assume that $\vec{A}_{\vec{R}}$ is constant over the region $\vec{R}$, the Laplace and the Nabla operator can be evaluated in Fourier space. We end up with the following expression for Eq. (16):

$$\mathbf{\Phi}(\vec{R}, z+\Delta z) \approx FT^{-1}\times\left\{\exp\left(\frac{i\Delta z(\hbar^2\vec{G}^2 + 2\hbar\vec{A}_{\vec{R}}\cdot\vec{G})}{2\hbar^2 k_0}\right)\times FT\left\{\exp\left(\frac{i\int(EV - V^2 - c^2\vec{A}^2 - c^2\hbar k_0 A_z)\,dz'}{2c^2\hbar^2 k_0}\right)\times\exp\left(\frac{i\int(e\hbar c\vec{\alpha}\cdot\vec{E} + e\hbar c^2\vec{\sigma}\vec{B})\,dz'}{2c^2\hbar^2 k_0}\right)\mathbf{\Phi}(R, z)\right\}\right\}. \quad (17)$$

This is the MS algorithm for fermions. Successive applications of Eq. (17), necessary for a proper scattering simulation of a thick specimen, yield the result of the wave function at the exit face of the crystal. The second exponential term is, according to the normal convention, called transmission function. For the same reasons the first exponential term is called propagator function, it is identical to the standard one. The last term has no counterpart in the standard formalism, it solely arises from the spinor nature of the wave function. It couples the different spinor components under the influence of electromagnetic fields. If electromagnetic fields occurring inside the specimen are sufficiently small, Eq. (17) can be approximated as

$$\Phi(R, z+\Delta z) = FT^{-1}\left\{\exp\left(\frac{i\Delta z(\hbar^2\vec{G}^2 + 2\hbar\vec{A}_{\vec{R}}\cdot\vec{G})}{2c^2\hbar^2 k_0}\right)FT\times\left\{\exp\left(\frac{i\int EV - V^2 - c^2\vec{A}^2 - c^2\hbar k_0 A_z\,dz'}{2c^2\hbar^2 k_0}\right)\Phi(R, z)\right\}\right\},$$

which would have occurred in the same way, if we had originally started with the Klein-Gordon equation and made the same derivations leading to Eq. (17). By neglecting V^2 the standard MS algorithm would be obtained.

We have to point out again that this solution does only work within the framework of forward scattering, the small angle approximation and a periodic vector potential $\vec{A}$. Furthermore, we have to slice the specimen into as small slices as necessary, assuring the validity of the Baker-Campbell-Hausdorff formula and the invariance of the derivatives in $\vec{R}$-direction with respect to z. In the next section, we will test the validity of the various approximations mentioned above, showing their nature explicitly.

6. Numerical calculations

For all three different relativistic expressions, i.e. Dirac, Klein-Gordon and approximated Klein-Gordon, numerical scattering simulations have been performed within the two numerical

approximations (numerical forward scattering, MS) on different crystal lattices in [100] zone axis orientation, namely Au ($Fm3m$, $a = 4.08$A), GaAs ($F\bar{4}3m$, $a = 5.65$A) and α-Fe ($Im3m$, $a = 2.87$ A). To show the explicit influence of the different expressions, no other contributions, e.g. those of the microscope or thermal motion of the atoms, have been incorporated. It should be noted, however, that in particular the thermal motion of the atoms have a rather large influence. In all simulations we use scattering potentials in the parametrization of Weickenmeier and Kohl [14], 300 kV acceleration voltage and a $128 \times 128 \times 128$ sampling of the unit cell. We will start with a comparison between Dirac, Klein-Gordon and approximated Klein-Gordon in the forward scattering formalism, i.e. Eqs. (10), (11) and (11) without the V^2 term, in the absence of magnetic fields (i.e. Au, GaAs), developed in Section 3. The incident wave was assumed to be a plane wave. The equations are solved by a Adams–Bashforth–Moulton PECE solver [15] implemented in the Matlab software suite [16]. The relative error of the solver was set to a sufficient low value of 0.0001. In Fig. 2 the modulus of an object exit wave of Au is depicted. The difference between object exit waves calculated by different algorithms can hardly be inspected visually, when looking on the real space images. It is, however, conveniently illustrated in the Fourier-transforms of the object exit waves by measuring the amplitude of certain plane wave components, referred to as beams. In Fig. 3 two different beams are depicted, the first one being the zero beam and the second one being a large angle scattering component taken from the first order Laue zone ([0,28] beam for Au, i.e. 135 mrad scattering angle; [5,21] beam for GaAs, i.e. 104 mrad scattering angle). There is no difference within the numerical accuracy between the Dirac and the Klein-Gordon simulations, which shows that spin effects are negligible. The neglecting of V^2 shows a very small influence below 0.1% in the high order reflexion. The difference is larger in the case of Au than in the GaAs, due to the stronger scattering potential of Au, it is however small compared to other previously mentioned approximations like the neglecting of inelastic scattering.

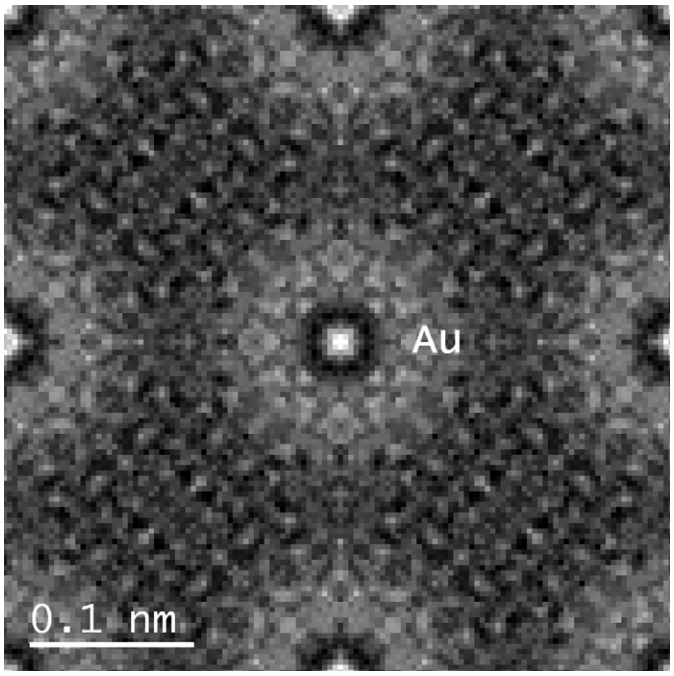

Fig. 2. Modulus of object exit wave of Au oriented in [100]-direction after a thickness of 25 unit cells. Acceleration voltage 300 kV, sampling rate $128 \times 128 \times 128$. The speckle is an effect of the discrete sampling.

Now we are going to compare the difference between the MS algorithm and the numerical forward scattering. The MS

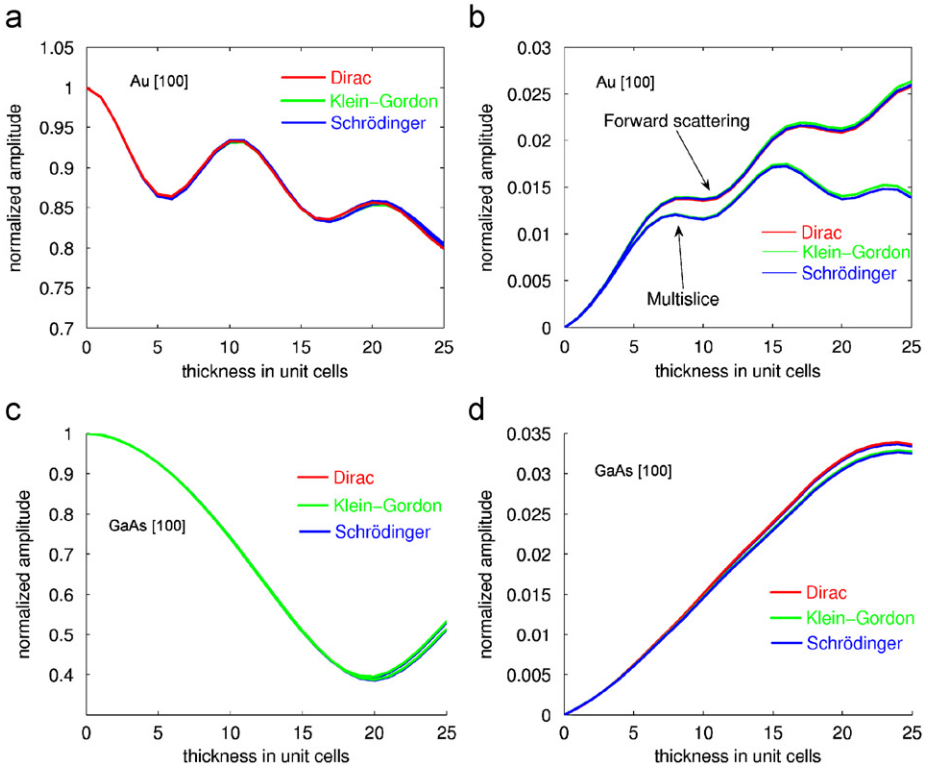

Fig. 3. [00] beam (a, c), [0,28] beam (b) and [5,21] beam (d) of electron waves scattered on Au (a, b) and GaAs (c, d). Acceleration voltage 300 kV, sampling rate $128 \times 128 \times 128$, zone axis [100].

simulations were performed with the same sampling rate like the forward scattering. Each atomic plane was contained in one slice. The difference is again illustrated by comparing the two previously used beams in Fourier-space. From Fig. 3 one can see that the difference in the small-angle scattering (zero beam) remains small contrary to large-angle scattering in the first order Laue zone. Again, the effect is larger in the case of the Au specimen, since more electrons are scattered into large angles and the scattering angle of the Au [0,28] beam is larger than that of the GaAs [5,21] beam. This difference in the large angle reflections follows from the small-angle approximation needed to derive the MS formalism (see discussion after Eq. (14), which is not valid for the scattering angles in the first order Laue zone ($\partial^2\Phi/\partial z^2 \approx k_{0z}\partial\Phi/\partial z$, i.e. the wave travels equally fast perpendicular to the incident direction as in the incident direction).

Finally we compare the scattering of spin-down $\mathbf{\Psi}_\downarrow$ and spin-up $\mathbf{\Psi}_\uparrow$ electrons on strong magnetic fields present in a deliberately chosen ferromagnetic material: α-Fe. The major part of the magnetic field within α-Fe is produced by the spin current density $\vec{j}_s$ of the partially filled d-shells. The splitting of the total current density $\vec{j}$ into a convectional and a spin part generally holds due to the Gordon transformation applied to the Dirac equation [12]. In the non-relativistic regime valid for the iron d-shell states, the spin part dominates and reads

$$\begin{aligned}\vec{j}_s &= \frac{e\hbar}{2m}\vec{\nabla}\times\mathbf{\Psi}^\dagger\vec{\sigma}\mathbf{\Psi}\\ &= \frac{e\hbar}{2m}\vec{\nabla}\times(\mathbf{\Psi}_\uparrow^\dagger\mathbf{\Psi}_\uparrow-\mathbf{\Psi}_\downarrow^\dagger\mathbf{\Psi}_\downarrow)\\ &= \frac{e\hbar}{2m}\begin{pmatrix}\frac{\partial}{\partial y}\left(\rho_\uparrow-\rho_\downarrow\right)\\ -\frac{\partial}{\partial x}\left(\rho_\uparrow-\rho_\downarrow\right)\\ 0\end{pmatrix}.\end{aligned}$$

The expressions assume a fixed polarization axis. The spin densities of iron are calculated within FPLO, an all-electron full-potential local-orbital implementation of density functional theory [17,18]. The laws of magnetostatics give the connection of the current density and the vector potential or the magnetic field.

$$\begin{aligned}\vec{A} &= \Delta\vec{j}_s,\\ \vec{B} &= \mathrm{rot}\vec{A}.\end{aligned}\tag{18}$$

The solution of Eq. (18) separates into the homogeneous part determined by the boundary conditions and the particular solution. The homogeneous solution is a wedge representing the macroscopic magnetic polarization of the sample. The macroscopic polarization of iron saturates at 1.7 T [19], thus can be safely neglected in comparison to the magnetic fields within the unit cell stemming from the particular solution (Fig. 4). When imaging large areas of the sample using medium-resolution electron microscopy, the enclosed magnetic flux produced by the macroscopic field, grows large enough to produce a significant signal though. The vector potential $\vec{A}$ calculated from Eq. (18) is now inserted into Eq. (10). Two spin polarized beams were separately calculated by preparing the starting conditions accordingly. Fig. 5 depicts the differences between the two differently polarized object exit waves. The difference is not visible and stays below 0.1%, indicating that the magnetic field does not couple to the spin of the wave on a microscopic length scale.

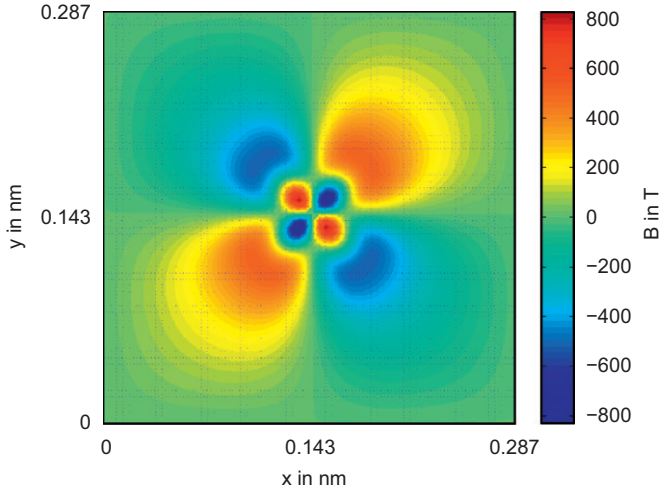

Fig. 4. Magnetic field B in z-direction at iron position.

7. Conclusion

We developed an extension to the standard multislice approach valid for the Dirac equation and investigated the influence of relativistic effects on electron scattering simulations. The validity of the standard formalism currently used in electron scattering simulations could be verified in case of practically all electromagnetic potentials present in the microscope. Even in the case of strong scatterers like Au atoms or ferromagnetic materials like α-Fe, the influence of the spin and the V^2 term stays small. The

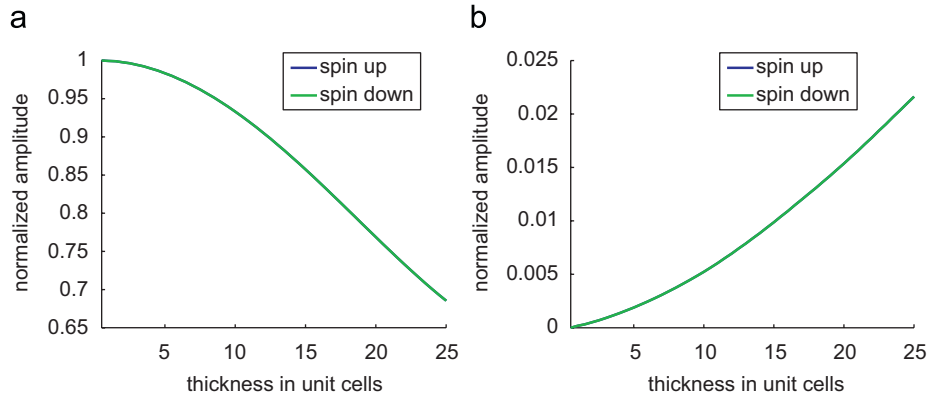

Fig. 5. [00] beam (a) and [0,14] beam (b) of electron waves scattered on iron. Acceleration voltage 300 kV, sampling rate 128 × 128 × 128. The difference between spin up and spin down are negligible and not visible.

error introduced by using the MS formalism instead of a numerical forward integration is more serious, in particular when regarding higher order reflections. If only small angle scattering is regarded like in HRTEM, the MS formalism yields equivalent results to the forward integration. If, however, large-angle scattered beams are measured, like in diffraction analysis under large-angle conditions (HAADF), the MS formalism might yield inaccurate results in particular when scattering on heavy atoms. Depending on the zone axis orientation and the sample thickness the error can reach several 10%. Unfortunately, the accurate numerical forward integration is computationally demanding and lacks an analytical incorporation of the thermal motion of the atoms. Thus, a realistic image simulation based on numerical forward integration would require time consuming frozen lattice summations [20], preventing a standard application of the formalism.

Acknowledgments

This authors acknowledge financial support from the European Union under the Framework 6 program under a contract for an Integrated Infrastructure Initiative. Reference 026019 ESTEEM. The discussion within the Triebenberg Lab is highly appreciated.

References

[1] J. Frank, Electron Tomography, Plenum, New York, 1992.
[2] K. Fujiwara, Relativistic theory of electron diffraction, J. Phys. Soc. Jpn. 16 (1961) 2226–2238.
[3] H.A. Ferwerda, B.J. Hoenders, C.H. Slump, Fully relativistic treatment of electron-optical image formation based on the dirac equation, Opt. Acta 33 (1986) 145–157.
[4] R. Jagannathan, Quantum theory of electron lenses based on the dirac equation, Phys. Rev. A 42 (1990) 6674–6689.
[5] L. Reimer, Transmission Electron Microscopy, Springer, Berlin, 1989.
[6] E. Kasper, P.W. Hawkes, Principles of Electron Optics, Vol. 3: Wave Optics, Academic Press, New York, 1995.
[7] P. Schattschneider, Fundamentals of Inelastic Electron Scattering, Springer, Berlin, 1986.
[8] W. Greiner, J. Reinhardt, Theoretische Physik 7: Quantenelektrodynamik, Verlag Harri Deutsch, Thun und Frankfurt am Main, 1984.
[9] P. Strange, Relativistic Quantum Mechanics, Cambridge University Press, Cambridge, 1998.
[10] E. Lamla, Zur Theorie der Elektronenbeugung bei Berücksichtigung von mehr als 2 Strahlen und zur Erklärung der Kikuchi-Enveloppen, Ann. Phys. 32 (1938) 178.
[11] W.H. Press, S.A. Teukolky, W.T. Vetterling, B.P. Flannery, Numerical Recipes in C, Cambridge University Press, Cambridge, 2002.
[12] W. Greiner, Theoretische Physik 6: Relativistische Quantenmechanik, Verlag Harri Deutsch, Thun und Frankfurt am Main, 1981.
[13] E.J. Kirkland, Advanced computing in Electron Microscopy, Plenum Press, London, 1998.
[14] A. Weickenmeier, H. Kohl, Computation of absorptive form factors for high-energy electron diffraction, Acta Crystallogr. A47 (1991) 590–597.
[15] L.F. Shampine, M.K. Gordon, Computer Solution of Ordinary Differential Equations: the Initial Value Problem, W.H. Freeman, San Francisco, 1975.
[16] Matlab. registered trademarks of The MathWorks, Inc.
[17] K. Koepernik, H. Eschrig, Full-potential nonorthogonal local-orbital minimum-basis band-structure scheme, Phys. Rev. B 59 (1999) 1743.
[18] H. Eschrig, M. Richter, I. Opahle, Relativistic Electronic Structure Theory, Part 2. Applications, Theoretical and Computational Chemistry, in: Relativistic Solid State Calculations, vol. 13, Elsevier, 2004, pp. 723–776.
[19] C. Kittel, Einführung in die Festkörperphysik, Oldenburg Verlag, Munich, 1999.
[20] R.F. Loane, P. Xu, J. Silcox, Thermal vibrations in convergent-beam electron diffraction, Acta Crystallogr. A47 (1991) 267–278.